Flood-Mapping

Release 0.1

IVillanueva

Mar 17, 2023

CONTENTS

Flood mapping and water bodies detection with the aid of computers and remote sensing imagery (satellites, airplanes and drones) requires cross-disciplinary but easy access information. The purpose of this online tutorial is to guide newcomers through the basic terminology with essential concepts and references, while they start capacity building or self-education programmes. All is based on the experience of over 12 international seminars in LATAM and MENA countries, face to face or remotely, and between 20-40 lecturing hours each, developed since 2017.

Note: The Chrome browser translation facility to spanish (ESP: usá el traductor de Chrome a español) has been proven right for this site. This project is under active development, promoted by ivillanueva.earth since March 2022.

CHAPTER

ONE

CONTENTS

1.1 Wet-Dry front dynamics

The Dam-Break problem or the breaking of a dam (Stoker, 1957) tracks the evolution of a reservoir and a downstream water column, both steady and with different heights initially, over ideal bottom conditions; flat and frictionless bed. Stoker showed there is an analytical or exact solution for the moving front: a simple “parabolic curve” when the downstream area is dry, and a more complex one when the downstream area is wet: [see figures]

Both problems are a good introduction to visualize the flooding dynamics of shallow water waves, although the complexity grows while natural conditions like irregular bottom (change of slopes) and friction or dissipation are considered. To solve “approximately” the front evolution and flood extent we need to discretize the conservation of mass and momentum, and apply numerical algorithms crunched by computer power, once the bottom is known (think of a digital elevation model with a pixel resolution with horizontal and vertical accuracies) and the boundary conditions for the flows are measured or typified (think of inflow hydrographs, dykes, sinks, free flowing, etc.)

At this early point it is important to think if your study case will need to evaluate the whole dynamics, with fronts or discontinuities moving across the domain of interest, with an accurate speed distribution, or you just need mean water depth values and maximum flood extents that can be solved with simplified schemes that are not so CPU demanding or can be simply monitored by Remote Sensing (RS) devices over specific periods of time. In other words it is essential to determine the temporary scale of your water body transient states, and the revisiting time of your RS devices.

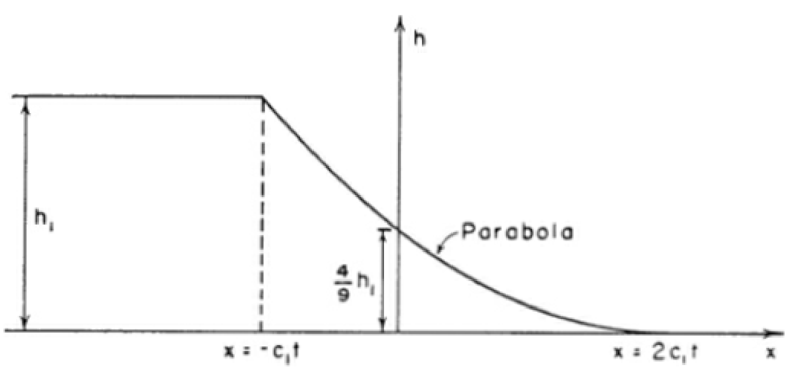

Fig. 10.8.5. Motion down the dry bed of a stream

Dam-break advance with speed $2c_1$ over flat, frictionless and dry bottom, being the celerity value $c_1 = \sqrt{gh_1}$ (really fast !)

Before the end of the 20th century the Mathematical concepts needed to deal with complex topography and fronts over dry beds were established, as we can see at this Milan symposium in 1994 by ASCE, which paved the road for the complete or full-hydrodynamic Saint Venant models we will practice with along this course.

Some typical scenarios where the whole dynamics is not essential, are rivers across large floodplains with many days of downstream routing, or when the available digital elevation model is coarse or not accurate, whereas the propagation of fronts and discontinuities is relevant in: flash floods, particularly in urban districts with affected surface drainage systems, narrow and steep valleys downstream dam structures breaching, tsunamis, etc.

1.2 Conservation laws and Domain meshing for numerical simulations

1.2.1 Mass and momentum conservation

Any conservation law for fluid motion can be expressed in conservative formulation as a partial differential equation (PDE), that in case of a depth-averaged model (shallow water equations or SWE) in a 2D or X-Y plane is written as:

$$\frac{\delta \bar{U}}{\delta t} + \frac{\delta \bar{F}}{\delta x} + \frac{\delta \bar{G}}{\delta y} = \bar{H}$$

Where U is the vector of conservative variables, F and G are flows in X and Y directions respectively, and H is a source term. For the complete 2D Saint Venant equations the terms are:

$$\begin{aligned}
\bar{U} &= (h, hU_x, hU_y)^T \\
\bar{F} &= (hU_x, hU_x^2 + \frac{1}{2}gh^2, hU_xU_y)^T \\
\bar{G} &= (hU_y, hU_yU_x, hU_y^2 + \frac{1}{2}gh^2)^T \\
\bar{H} &= (0, gh(So_x - Sf_x), gh(So_y - Sf_y))^T
\end{aligned}$$

Symbol	Variable and dimension	Symbol	Variable and dimension
h	water depth (m)		
Ux	X-velocity (m/s)	Uy	Y-velocity (m/s)
Sox	X-Slope (no dim)	Soy	Y-Slope (no dim)
Sfx	X-friction slope (no dim)	Sfy	Y-friction slope (no dim)
g	gravity constant (m/s^2)		

The differential solvers are evaluated across neighbouring cells of a domain or mesh, that historically have been evolving from quadrilateral to triangular shapes. As first example, the raster based approach used by Lisflooood-FP is presented:

1.2.2 Type of mesh

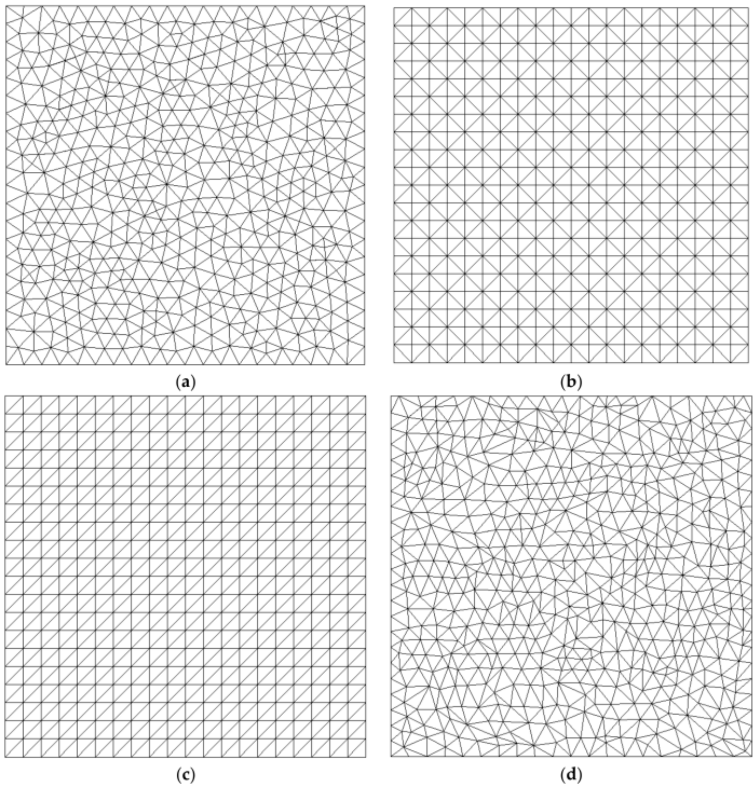

Figure 15. Four triangular mesh types used for computation: (**a**) Delaunay; (**b**) orthogonal-I; (**c**) orthogonal-II; (**d**) distorted.

Triangular based meshes for 2D domains, to discretize the mass and momentum differential equations. As example, the non-structured triangle based approach used by RiverFlow2D, a Delaunay tessellation:

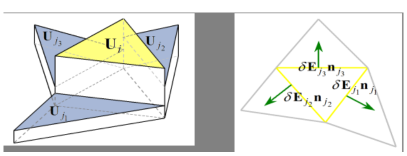

1.2.3 Practical approach: hybrids

The river main channel interaction with the floodplain by overtopping embankments or levees can be modelled using a combination of cells (quadrilateral or triangular) which will require higher density of cells in the transitions or when the speed pattern is expected to be more complex or less uniform in space. The whole domain can be seen as a 1D conduit plus a 2D plain:

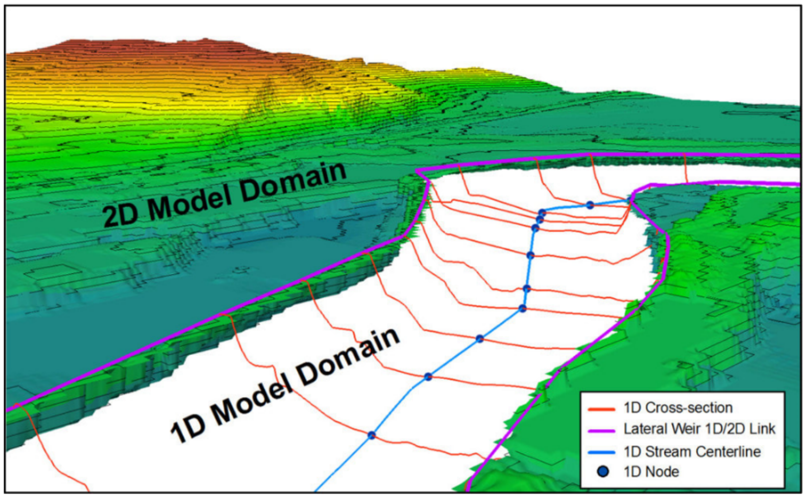

Or as a complete 2D domain, which is easier to config and more stable, but demands more memory and CPU time. For instance RSH-2D (US Bureau of Reclamation, 2008) combines quadrilateral cells along the main channel and levees but mixed coarser cells at the plains.

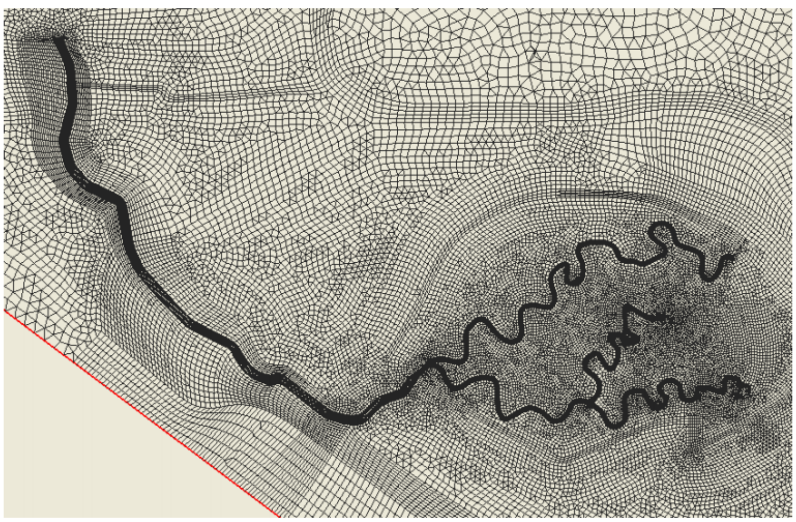

Or the widespread non-structured triangular mesh for the whole domain, also known as flexible mesh, note the finest resolution around levees, by TELEMAC model.

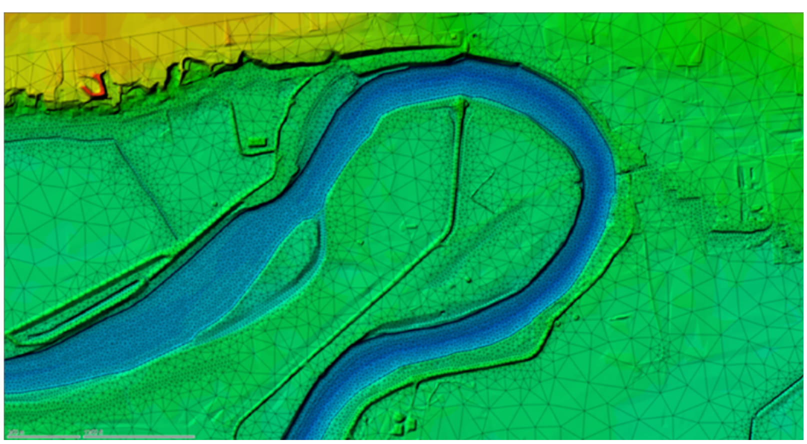

Detailed 3D view of a flexible mesh around levees and dykes, by Iber model:

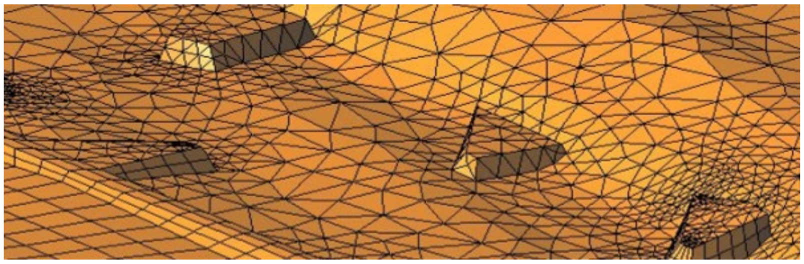

In the presence of building blocks, with no porosity, the grids are adapted to the free flood ways, as seen in this HEC-RAS example which uses breaklines as axis for the streets:

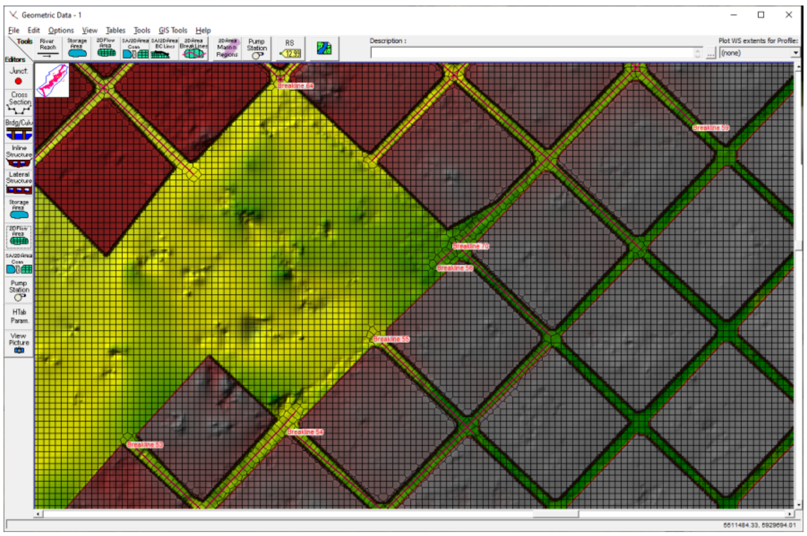

1.2.4 The Time Step issue

For an orthogonal or cartesian meshed domain Ω , the Courant-Friedrichs-Levy criteria defines a CFL coefficient that linearly limits the time-step, multiplied by the cell size, and divided by the sum of flow speed and celerity:

$$\Delta t_{x,y} = CFL \frac{\Delta x, y}{|U_{x,y}| + \sqrt{gh}}$$

$$\Delta t = min(\Delta t_x, \Delta t_y)_\Omega$$

Note that if $(\Delta x, y \ll, U_{x,y} \gg, h \gg) \implies \Delta t \to 0$

The time-step governs the mass conservation at every control-volume or cell, for instance in 2D(X, Y):

$$\frac{\delta h}{\delta t} + \frac{\delta(hU_x)}{\delta x} + \frac{\delta(hU_y)}{\delta y} = 0$$

Whereas we go deeper with the simpler 1D(X) formulation:

$$\frac{\delta A}{\delta t} + \frac{\delta Q}{\delta x} = 0$$

Which can be discretized (super-index ‘n’ stands for evolution in time and sub-index ‘i’ for location in 1D-grid) in an explicit way, like the Euler scheme :

$$\frac{A_i^{n+1} - A_i^n}{\Delta t} + \frac{Q_{i+1/2}^n - Q_{i-1/2}^n}{\Delta x} = 0$$

Called explicit because the value at ‘n+1’ can be formulated joining only known terms at ‘n’ on the right hand side:

$$A_i^{n+1} = A_i^n + \frac{\Delta t}{\Delta x}\left(Q_{i-1/2}^n - Q_{i+1/2}^n\right)$$

Which allows for stability if $CFL1$

Whereas an implicit discretization scheme, like the box-scheme:

$$\frac{\left(\Psi A_{i+1}^{n+1} + (1-\Psi)A_i^{n+1}\right) - \left(\Psi A_{i+1}^n + (1-\Psi)A_i^n\right)}{\Delta t} + \frac{\Theta\left(Q_{i+1}^{n+1} - Q_i^{n+1}\right) + (1-\Theta)\left(Q_{i+1}^n - Q_i^n\right)}{\Delta x} = 0$$

With spatial weight $0 \leq \Psi \leq 1$, and implicit parameter $0 \leq \Theta \leq 1$ allows for stability even with $CFL1$

The price for an implicit scheme, as briefly seen, is that the solving algorithm and coding are more complex but the execution can be faster, depending also on the domain mesh division and its hardware distribution among processing units (CPU, GPU or TPU). Particularly, the popular HEC-RAS code uses an implicit scheme formulation.

Note we did not consider the conservation of momentum, for the sake of simplicity in the formulation. To know more visit[]

1.2.5 Simulation mass balance

One overall value to check at the end of every simulation is the mass conservation applied to the entire domain for accounting the difference of volume, and all the inflows and outflows across the boundaries.

$$V^T - V^0 = \sum_k Q_{in}^k \Delta t_k - \sum_k Q_{out}^k \Delta t_k$$

Where

$$V^n = \sum_\Omega h_{ij}^n \delta x_i \delta y_j$$

1.2.6 Benchmarking software:

The links and credits for the referred software are:

HEC-RAS, USACE

Iber, UDC UPC CEDEX

Lisflood-FP, U. Bristol

RiverFlow2D, GHC U. Zaragoza & Hydronia Ltd

RSH-2D, US Bureau of Reclamation

TELEMAC, Global consortium

1.3 Digital Elevation Models

1.3.1 Common sources and vertical accuracy

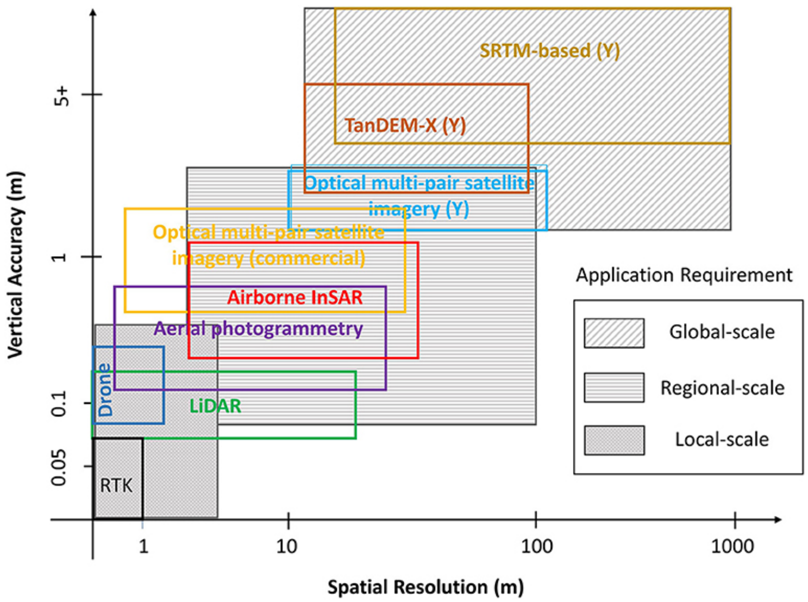

DEMs: spatial resolution and vertical accuracy for different RS techniques and scales of application. From Schumann & Bates, 2018

1.3.2 DSM filtering to obtain DTM

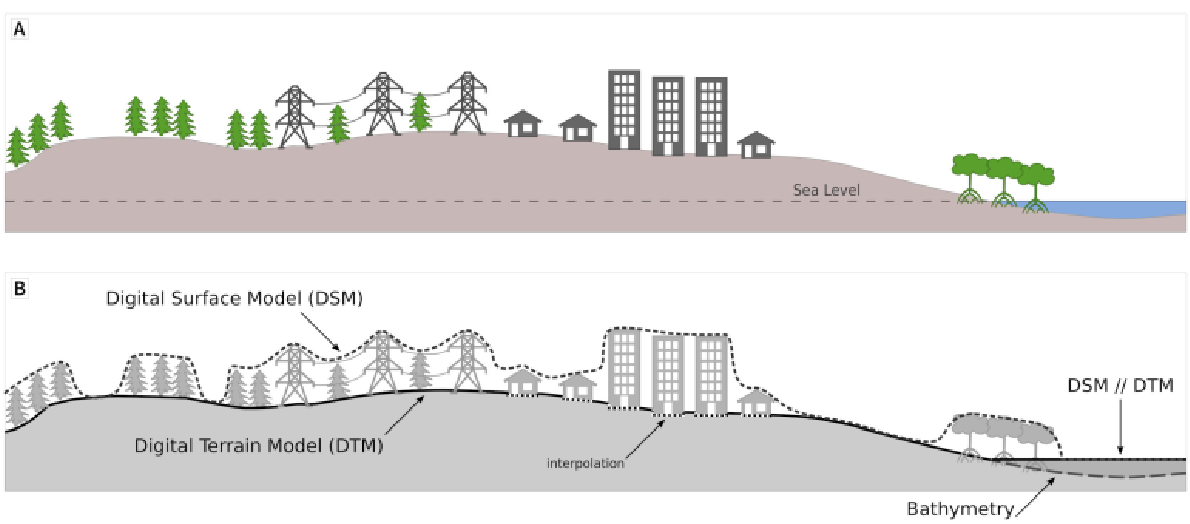

Digital Surface Model versus Terrain Model in "Terminology and Definitions for Digital Elevation Models", Guth et al, 2021.

To understand how to transform a DSM from a Remote-Sensing device, as simple and affordable as a drone camera, in optical range (no LiDAR nor laser detection), we describe briefly the principles to generate a cloud of points from geo-referenced pictures (SfM: structure from motion), the 3D building of the surface model (dense multi-stereo matching) and the filtering with a SMRF (Simple Morphological Filter) to remove basically vegetation and blocks to work with bare earth.

Structure from motion principles and dense reconstruction

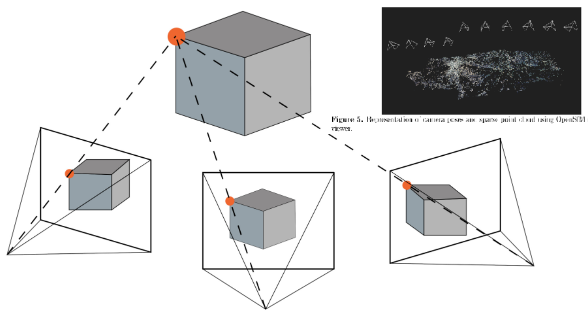

The SFM problem. What kind of camera took these pictures and where was the camera when the pictures were taken?

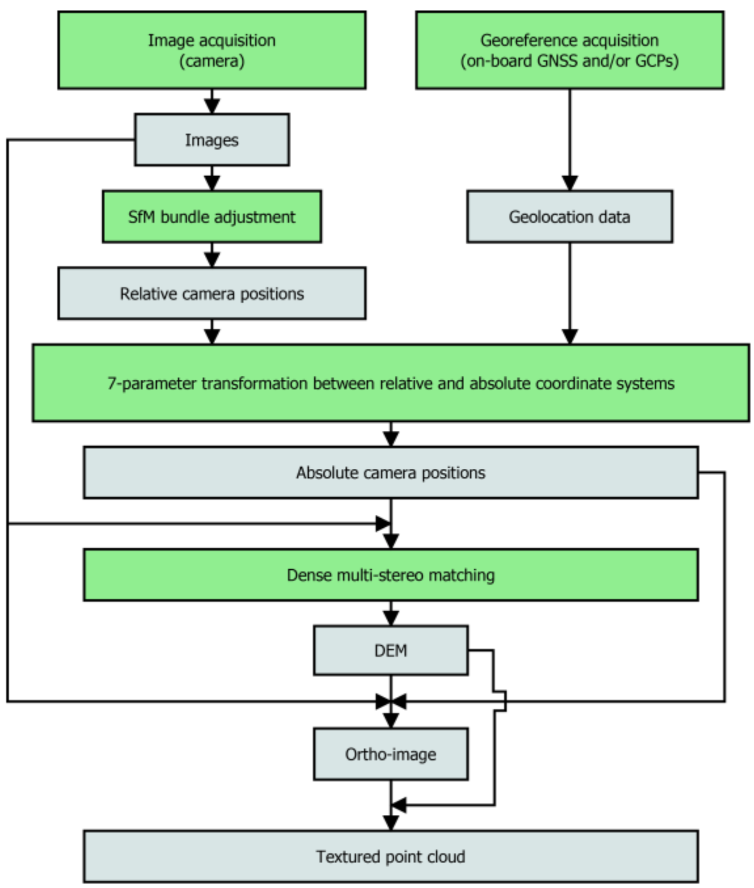

Figure 1. Standard SfM photogrammetry processing workflow. Green boxes are processing steps and grey boxes are products.

The workflow comes from the selected reference of Girod et al, 2017.

Filtering with SMRF windows

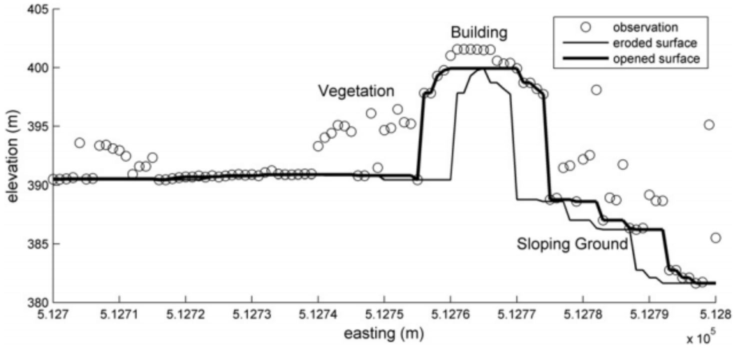

How a surface or a cloud of points is eroded with a SMRF filter using different slopes, or window height and length parameters, by Pingel et al, 2013. And how the parameters are tunned with smrf ODM-flags.

1.3.3 Training with affordable drones

In this section we practice with High-Quality drone imagery and the Open-Drone-Map software (ODM), to obtain DSMs and DTMs from simple flights to set the essential ground data for reliable simulations, at scales of a few hectares.

The basic documentation for processing a package of photographs from a drone flight can be reached at docs-opendronemap.

A repository with significant packages to start training, like the Carossio quebrada at Lima, Perú, IAPG-2022 training, will be available soon.

1.4 Large Scale Modelling assisted by Satellite imagery and Artificial Intelligence

While monitoring large areas or tiles of several hundred Kilometers, with pixel size over 25 meters, it is convenient to reduce the complexity of the shallow water equations (SWE) in order to allow larger time-steps for numerical simulations at the expense of loosing accuracy for the speed field pattern or wave propagation time. The objective for Large Scale Modelling (LSM) is to maintain critical information like the maximum flood extent and its duration, but none about highly transient states nor dynamics related to fine grid resolutions: trans-critical flows, overtopping, sediment transport and bed river evolution, pollutant dispersion, etc.

1.4.1 Difussion-Wave or Zero-Inertia approximation

The momentum conservation at every control-volume or cell for the full (or complete) SWE equations, 1D(X) case, states:

$$\frac{\delta Q}{\delta t} + \frac{\delta\left(Q^2/A\right)}{\delta x} + gA\frac{\delta\left(Z_b + h\right)}{\delta x} + gAS_f = 0$$

Symbol	Variable and dimension	Symbol	Variable and dimension
Q	discharge (m^3/s), Q=Av	A	area (m^2)
Zb	bed level (m)	h	water depth (m)
Sf	friction slope (no dim)	g	gravity constant (m/s^2)

Can be adapted (or adopted) for LSM considering the inertial (or acceleration) terms vanish:

$$\frac{\delta Q}{\delta t} \to 0$$

$$\frac{\delta\left(Q^2/A\right)}{\delta x} \to 0$$

Or equivalently:

$$\frac{\delta h}{\delta x} - S_0 + S_f = 0$$

That links friction slope with stage gradient, as the bed slope is

$$S_0 = -\frac{\delta Z_b}{\delta x}$$

Using empirical Manning´s formulation with 'n' as roughness coefficient, 1D(X) or 2D(X, Y):

$$S_f = n^2\frac{Q\left|Q\right|}{A^2R^{4/3}},\ S_{fx,y} = n^2\frac{U_{x,y}\sqrt{U_x^2+U_y^2}}{h^{4/3}}$$

allows to define the intercell discharge 'q'. For instance, the 2D code Lisflood-FP uses

$$q_{i+1/2}^{n+1} = \frac{(h_f^n)^{5/3}}{n}\nabla(Z_b+h^n)_{i+1/2}^{1/2}$$

With the flow-depth as

$$h_f^n = max\left((Z_b+h^n)_i, (Z_b+h^n)_{i+1}\right) - max\left((Z_b)_i, (Z_b)_{i+1}\right)$$

And an interesting implicit version

$$q_{i+1/2}^{n+1} = \frac{q_{i+1/2}^n - gh_f^n\Delta t\nabla(Z_b+h^n)_{i+1/2}}{1+g\Delta t\frac{n^2\left|q_{i+1/2}^n\right|}{(h_f^n)^{7/3}}}$$

See for more details Neal et al, 2012 .

1.4.2 Satellite Optical and IR bands to detect water bodies: MNDWI index

The combination of bands that defines the Modified Normalized Difference Water Index (MNDWI) is visible green (537-582 nm) and short-wave infrared (1539-1681 nm), that in case of the Sentinel-2 MSI are B3 and B11 respectively:

$$MNDWI = \frac{B_3 - B_{11}}{B_3 + B_{11}}$$

See for more details Cordeiro et al, 2021 .

It is a relatively easy way of processing and detecting water surfaces over a certain "MNDWI" threshold value, coping with bimodal pixel distributions and the Otsu optimal threshold, in fact the problem is to detect accurately the dry-wet boundaries, and there the computational vision techniques for noise filtering and edge detectors play a major role. See the practical case with Google-Earth-Engine for Paso de las Piedras reservoir, Bahía Blanca, Argentina.

1.4.3 Altimetry fundamentals

Apart from a flood or water body extent, satellite signals can measure water surface elevations too, in order to understand the signal processing we review the main concepts to determine the water surface elevation as:

$$h_{WSE} = H_{Sat} - (R_0 + R_{Dry-tropo} + R_{Wet-tropo} + R_{Iono}$$
$$+R_{Solid-Earth-Tide} + R_{Pole-Tide} + R_{Geoid}$$

Considering corrections due to instruments, propagation and geophysical factors. The figure displays the footprint for an altimetry mission with Synthetic Aperture RADAR (SAR) signal and its typical resolution along-track axis.

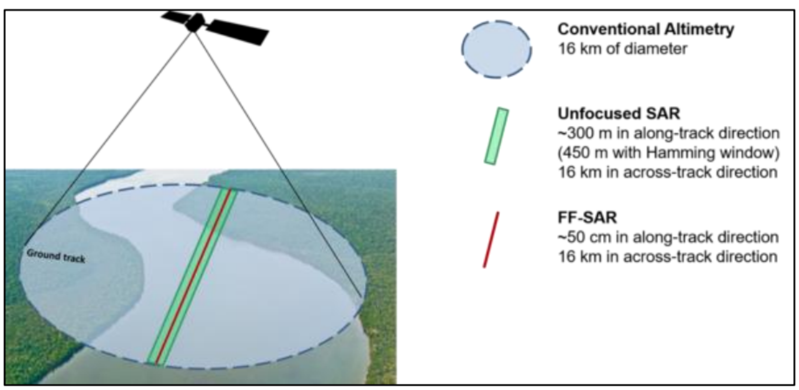

1.4.4 Image processing: noise filtering

Multi-Spectral and Panchromatic imagery are subject to the presence of cloud cover, whereas SAR microwaves are not perturbed. For the former group access to pre-event images or filtering techniques are needed. The presence of vegetation over water bodies is a common and frequent source of noise for any exploitation of remote sensing imagery. SAR imagery researchers and practitioners continue improving algorithms to identify water bodies under vegetation or between buildings, considering effects like double bounce and shadows for the backscatter, that depend on the wavelength, polarisation and incidence angle, and of course the surface roughness and dielectric properties, but those SAR processing techniques are out of the scope of this basic manual.

1.4.5 Image processing: edge detectors and buffers

To locate the wet-dry boundaries a 2D convolution operator is set to identify that particular pattern across the domain, this is an image processing technique commonly used, that for every pixel of the domain weights the surrounding pixels according to a defined Kernel. For instance to detect a North dry-wet edge, a 3x3 kernel can be set to {[1, 1, 1], [-1, -1, -1], [0, 0, 0]} and subsequently applied to a MNDWI or back-scatter water surface layer, to detect negative values below a threshold which are candidates to represent a North dry-wet bound.

The following image summarizes the action of a Kernel (Sobel-Gaussian) filtering over a source image:

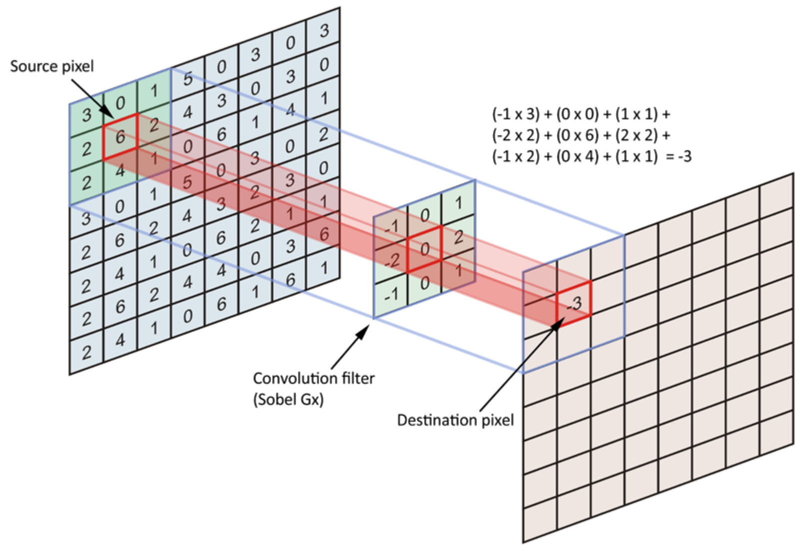

In order to estimate the water depth related to the water surface recorded by satellite imagery (with no altimetry, ie Multi-Spectral or SAR backscatter), a base DTM or raster elevation is needed, where the 2D-convolution operator is applied using a Kernel that weights the terrain neighbours to have a mean value of the bottom, adding a special treatment to have extra-accuracy at dry-wet boundaries, river banks or embankments, to serve as reference for the water surface height.

1.4.6 Image analysis: RS change detection synergy with Deep Learning from Simulations

Starting with semantic segmentation at pixel level from remote sensing images, and training with Deep-Learning frameworks using Convolutional Neural Networks (CNN), in particular U-Net, fed by numerical simulations, we describe the process to create synthetic data scenarios for training through simulation that will resemble real change scenarios monitored by remote sensing, and need some completion because of missing data, inconsistencies, false negatives, etc. Of course this is a considerable task and the simple purpose here is to understand the setting up, a complete reference is the work by Yokoya et al.

At this point is useful to describe a metric for comparison or change detection between multi-temporal images or simulations, the Jaccard index (intersection over union):

$$J(I_{mg}, S_{im}) = \frac{I_{mg} \cap S_{im}}{I_{mg} \cup S_{im}} = \frac{I_{mg} \cap S_{im}}{I_{mg} + S_{im} - (I_{mg} \cap S_{im})}$$

$$0 \leq J(I_{mg}, S_{im}) \leq 1$$

A Jaccard value of one means identical extents, whereas a value of cero means null intersection. If the two rasters have the same number of pixels (Nx, Ny) and equal frame coordinates, the index can be calculated as:

$$J(I_{mg}, S_{im}) = \frac{Sum(I_{mg} * S_{im})}{Sum(I_{mg}) + Sum(S_{im}) - Sum(I_{mg} * S_{im})}$$

Where Sum is the addition of all the pixels (Nx, Ny) values.

1.4.7 Setting up a Convolutional Neural Network like U-Net

A CNN U-Net with Attention Gates can be set up in a few lines of code with the open source PyTorch libraries.

The basic theory, states that a CNN is trained to minimize the difference between a forwarded input image (time n, domain Ω_1) and a further reference image (time n+T, domain Ω_2), for a set of K training pairs, being the loss to minimize:

$$Loss = \sum_K \left(Fwd_{CNN}(Img^n_{K,\,\Omega_1}), Img^{n+T}_{K,\,\Omega_2} \right)_{metric}$$

The Forward-CNN engine or predictor, is a substitute for a physically based simulation, in our case, the selected configuration applies four “convolutional+pooling” downsampling layers, and afterwards another four upsamplings (U-shape) connecting with attention gates, layers of the same Width-Height, and for simplicity an identical domain Ω. The metric can be the Jaccard index (intersection over union), RMSE or LSHI, the last two applied to flatten rasters. During the live course how to select images and the training set up are discussed in detail, at this point the whole process can be summarized with the following steps:

1. Selection of Imagery from selected scenarios and significant simulations or remote sensing layers, a careful process to select a proper set number with direct risk impact.
2. Imagery loading and further transformations in order to be processed by Pytorch libraries and optimization engines.
3. Training of the selected CNN configuration to optimize the Forward-Step or predictor operator.
4. Testing with selected events to improve the prediction capacity and reach Real-Time feasibility.

As indicative figures, a typical Set-Up might require a CNN with as much as 57 M parameters to optimize, for a mosaic of 100 training images, and run in a few minutes both for training and prediction with Graphical Processor Units (GPU).

Figure of the U-Net architecture as pictured by Iglovikov, 2017

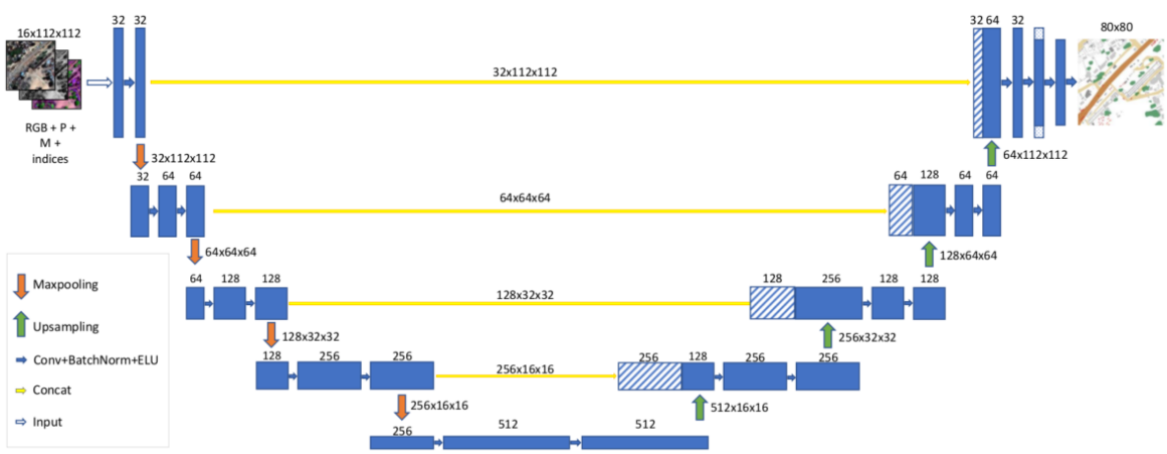

1.4.8 Global surface water mapping

To have a reference for change detection anywhere, worldwide databases with the extent of permanent water bodies and their time variability are available at the JRC database, and Global-Flood.

1.5 Google-Earth-Engine practical cases

To illustrate the use of the discussed terminology for satellite imagery processing, a few cases have been selected. A Google-Earth-Engine account is required to map and process the data.

Link to GEE available datasets, including Sentinel 1 & 2 imagery, SRTM-DTM, and many other data bulks.

1.5.1 Worldwide databases

The JRC and the Global-Flood databases for permanent water bodies and their fluctuations, are also available at GEE.

1.5.2 San Pedro Sula, Honduras, November 2021, post-hurricanes effects

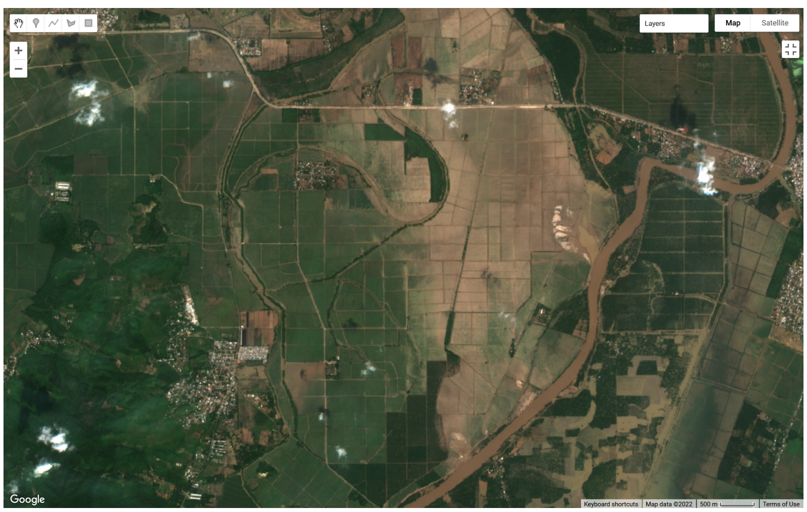

1.6 Drones + LSPIV: local flow-speed measurements

In this section we practice with High-Quality drone imagery and the RIVeR software (RIVeR), based in PIV-lab.

LSPIV processing of drone captured videos, allows to detect and measure river flow patterns, like this recirculation as a result of an expansion, downstream a dyke.

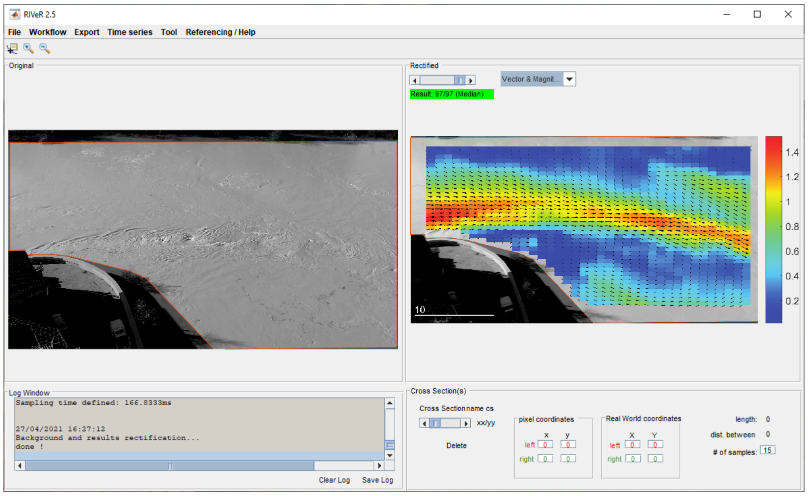

1.7 Post-flood disaster evaluation study

As example to show how the discussed technologies are combined in order to evaluate and manage a post-flood scenario, a study case is analysed: The Melamchi Flood Disaster in Nepal, June 2021, covering Damage and Risk Quantification with Drone Survey, Satellite-Based Land Displacement Analysis, and 2D Flood Modeling, from the original World-Bank report.

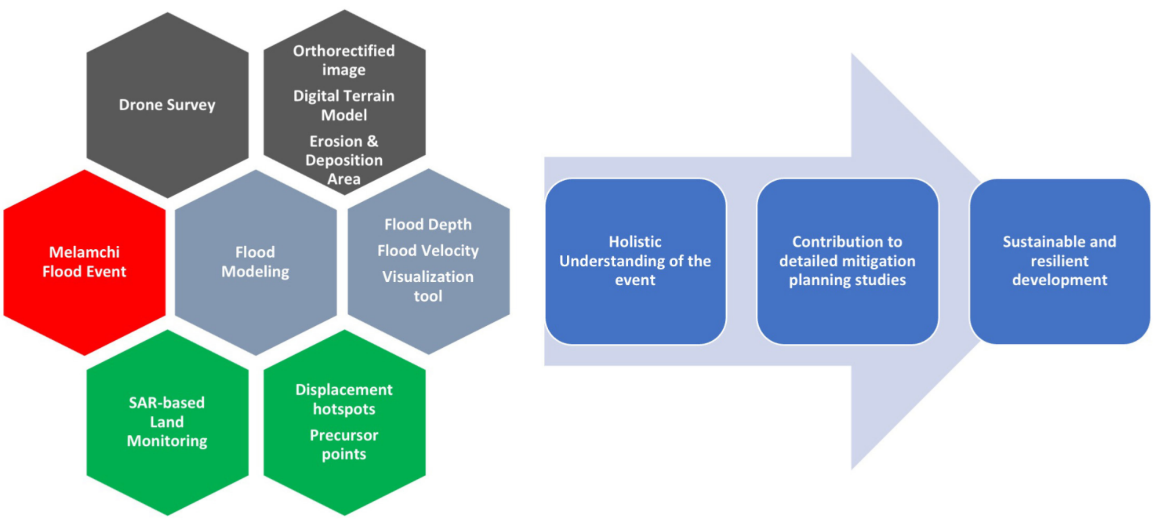

1.8 Concluding remarks and what's next

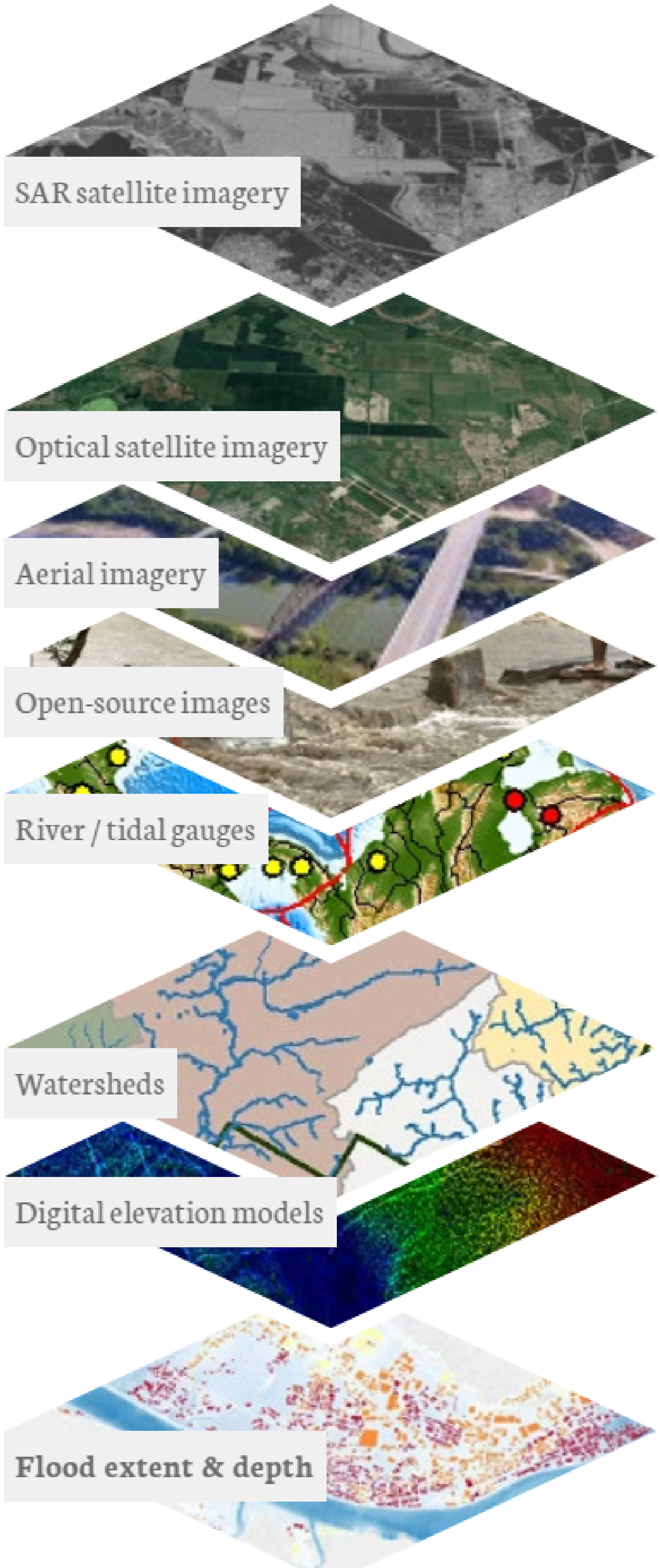

All the involved layers within a Decission Support System to monitor flood inundation, and short term evolution (by ICEYE.com).

1.8.1 Remote Sensing Mapping vs Numerical Modelling

1.8.2 Real Time Integration: Early Warning Systems

1.9 Historical reviews

As stated by Stoker , in "Water Waves: The Mathematical Theory with Applications", since 1957 it is clear and feasible to make predictions of floods in rivers knowing the state of the river at some initial instant, and the observed-estimated or forecasted, flow into the river from its tributaries and the local run-off, through the basic differential equations we have roughly presented, and their associated numerical solutions solved by computers.

After more than 60 years of Stoker practices, the digital era with open access RS data and affordable computing processors, has popularized the Flood-Mapping science, a state of the art methodology can be found in "Flood Inundation Prediction" by Bates, 2022, being the main challenges to face:

- Rationalize and properly select among the considerable bulk of observational data, including the imagery to validate predictions.
- Match the numerical engine which describes best the physical process, to the available terrain model (resolution and accuracy) and temporal scales, assuming the computational cost. In general relaxing the grid resolution to coarse pixels, allows to validate more parameters and scenarios, that for large scale hazard mapping related to Climate Change is very relevant, but non-appropriate for local hydraulic modelling.

1.9.1 Scanned images

Flood modelling is not only about choosing an appropriate mesh and numerical solver, the topology and connections between hydraulic structures play a major role, we rediscover here the concept of "breakline" for the river axis and its flow distribution across plain cells, by Giammarco and Todini, 1994, when numerical engines started to couple with Geographical Information Systems or GIS frameworks.

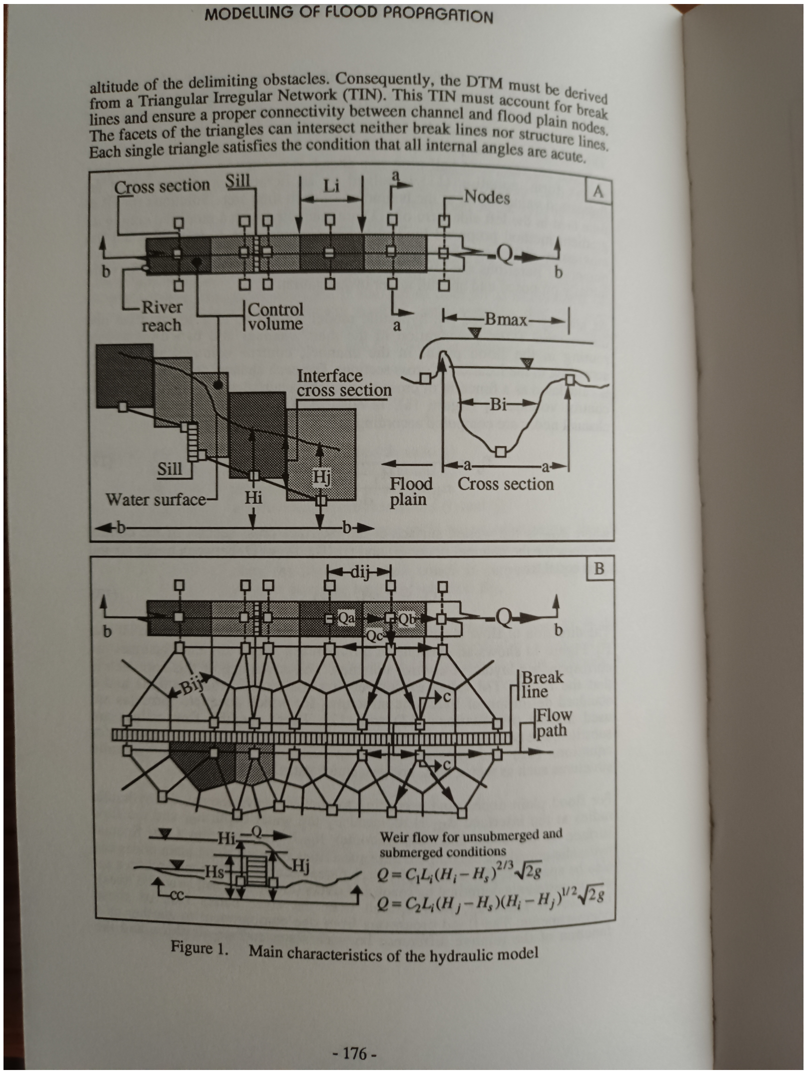
MODELLING OF FLOOD PROPAGATION

altitude of the delimiting obstacles. Consequently, the DTM must be derived from a Triangular Irregular Network (TIN). This TIN must account for break lines and ensure a proper connectivity between channel and flood plain nodes. The facets of the triangles can intersect neither break lines nor structure lines. Each single triangle satisfies the condition that all internal angles are acute.

Figure 1. Main characteristics of the hydraulic model

- 176 -

1.10 Operational issues and appendixes

In this section a few operational or more practical issues, like tables, "how-to" hints or frequently asked questions, software tricks or demos are explained in a more detailed way.

1.10.1 Hazard and Risk mapping

Directly associated to flood simulations, or frequently the promoter, is the calculation of the Flood Risk, nowadays strongly linked to Climate-Change scenarios.

The Risk is a function of Hazard, Exposure, and Vulnerability, being:

1. Hazard, with two components:
    - Intensity: direct result of simulations that output rasters with Water Depth, Velocities, and Extents.
    - Probability of hazard: linked to the Return Period of the forcing boundary: a river discharge for fluvial floods, a rainfall for pluvial floods, or the sea level for coastal floods.

2. Exposure: related to accounting Land Uses, type of buildings and infrastructures, all analysed within a GIS Framework. Nowadays a correct and affordable pixel resolution for Risk calculations is as fine as 1-2 meters.
3. Vulnerability: through the damage curve that relates usually Water Depth versus Damage having particular dependencies on the physical structures or terrain contents, if the loss is direct or indirect, tangible (economic loss) or intangible (population, injuries or loss of life).

Tipically a Total-Damage is calculated as a sum over Polygons, considering an averaged Water-Depth(WD) over each surface Polygon (S):

$$TD = \sum_{Polygs} S_{Polyg} V_{Max-Dmg} \Theta_{Polyg}(\overline{WD})$$

A more complex analysis can be held by using the product of Depth times Velocity, specially when it is directly applied to population or cars, using the so called vulnerability curves.

Annual Expected Damage:

The expected annual damage (EAD), also known as averaged annual damage (AAD), although the former is more used to predict, is the average of flood damages calculated over a number of events, where the total damage for each event is weighted by its probability in a year, that weight can be:

$$W_i = 1. - exp\left(\frac{-1}{T_i}\right) \; or \; W_i = \frac{1}{T_i} - \frac{1}{T_{i+1}}$$

1.10.2 Tabulating validation data sources

From Bates, 2022, we can extract a table with the most common sources and ranges for model validation.

Data type		Known typical errors and limitations
Gauged discharge		±10–20% for medium or high in-bank flows and up to ±40% for out-of-bank flows
Water level	Gauging station	±0.01–0.02 m
	Post-event wrack or water mark	±0.3–0.5 m on average, but with a possibility of more extreme outliers
	Satellite radar altimetry (e.g., ICESat, Jason, Topex/Poseidon, CryoSat-2, Sentinel-3)	0.05–1.5 m (RMSE), but most instruments were designed for oceanic or cryosphere applications and thus have large ground footprints (~70–600 m) and/or unusual orbits. Such data are therefore predominantly limited to use on larger rivers.
	Satellite radar interferometry (e.g., L-band radars such as JERS-1, ALOS PALSAR)	Typically a few centimeters, although to date this approach can only be used to determine water levels beneath flooded vegetation (e.g., in the Amazon and Congo floodplains). This will change with the launch of the SWOT satellite mission scheduled for 2022 (**https://swot.jpl.nasa.gov/**).
	Airborne radar interferometry (e.g., AirSWOT Ka band radar)	RMSE of ~0.1 m compared with 12 ground pressure transducers along a ~90-km reach of the Tanana River, Alaska
Water velocity	Current meter	2% in laboratory tests, likely higher error (perhaps 5–10%) under field conditions
Flood extent	Air photo	Flood shorelines can be geolocated to within 10–100 m, but often through a manual process. This gives inundated area to perhaps 5–10% of true value at best, although accuracy is reduced for oblique rather than vertical imagery. Illumination conditions can also significantly affect image processing.
	Optical satellite image (e.g., Planet Labs, MODIS, Landsat)	Various resolution data available from ~meters to ~kilometers, with trade-offs between resolution, sampling frequency, and ground track width. Operation is restricted to daytime and images can be affected by cloud cover. Robust accuracy assessment is limited but can perhaps map inundated area to 20–30% of true value under good conditions. Large local deviations from truth are probably typical.
	SAR image (e.g., ERS, Radarsat, Sentinel-1b, COSMO-SkyMed)	Imaging radars are usually X- and C-band instruments capable of day–night, all-weather operation. Typical resolutions are in the range of 3 to 30 m, and mostly long spacing between orbit revisits (10–30 days) as a result. Comparison of simultaneous air photo and SAR imagery of a flood in the United Kingdom shows radar data can capture 75% of true flooded area, so accuracy similar to that of optical satellite imagery and large local deviations from truth are also probably typical.

1.10.3 Urban scenarios: street meshing

While working with building blocks across urban scenarios, the most accurate and flexible approach for meshing is the Delaunay tessellation, in this case with GMSH mesh generator. The steps will be described during a live course.